Binder-free all-carbon composite supercapacitors

Binder-free all-carbon composite supercapacitors

To cite this article before publication: Sabreen Jarrar *et al* 2024 *Nanotechnology* in press https://doi.org/10.1088/1361-6528/ad41e9

Binder-free All-Carbon Composite Supercapacitors

Sabreen Jarrar[a], Shahzad Hussain[b*], Atta Ul Haq[b], Gourav Bhattacharya[b], Iyad Saadeddin[a], Llorenc Servera[c], JM Ruiz[c], Alaa Janem[d], Allan Daraghmeh[a*]

[a] *Department of Physics, An-Najah National University, P.O. Box 7, Nablus, West Bank, Palestine*

[b] *Nanotechnology & Integrated Bio-Engineering Centre (NIBEC), Ulster University, Shore Road, Newtownabbey BT37 0QB, United Kingdom*

[c] *Escola Universitaria Salesiana de Sarria (EUSS), Passeig Sant Joan Bosco,74, 08217 Barcelona Spain*

[d] *Department of chemistry, An-Najah National University, P.O. Box 7, Nablus, West Bank, Palestine*

E-mail address: allan.d@najah.edu (A. Daraghmeh[a*])

E-mail address: sha.awan@hotmail.com (S.Hussain[b*])

Abstract

Carbon-based electrode materials have widely been used in supercapacitors. Unfortunately, the fabrication of the supercapacitors includes a polymeric binding material that leads to an undesirable addition of weight along with an increased charge transfer resistance. Herein, binder-free and lightweight electrodes were fabricated using a powder processing of carbon nanofibers (CNFs) and graphene nanoplatelets (GNPs) resulting in hybrid all-carbon composite material. The structural, morphological, and electrochemical properties of the composite electrodes were studied at different concentrations of GNPs. The specific capacitance (Cs) of the CNFs was improved by increasing the concentration of GNPs in the composite. A maximum Cs of around 120 F g^{-1} was achieved at 90 wt.% GNPs which is around 5-fold higher in value than the pristine CNFs in 1 M KOH, which then further increased to 189 F g^{-1} in 6 M KOH electrolyte. The energy density of around 20 Wh kg^{-1} with the corresponding power density of 340 W kg^{-1} was achieved in the supercapacitor containing 90 wt.% GNPs. The enhanced electrochemical performance of the composite is related to the presence of a synergistic effect and the CNFs establishing conductive/percolating networks. Such binder-free all-carbon electrodes can be a potential candidate for next-generation energy applications.

Keywords

Binder-free; Carbon nanofibers; Graphene nanoplatelets; Nanocomposite; Energy storage, Supercapacitor

1. Introduction

Supercapacitors are an efficient candidate for sustainable and greener energy storage systems due to their outstanding features like high-power densities, cyclic stability, reliability, and safety [1]. The performance of a supercapacitor highly depends on the type and characteristics of the electrode materials. Typically, the electrode materials can be classified into several types or groups such as carbon materials [2, 3, 4], metal oxides [5, 6, 7], conducting polymers [8, 9], and MXENS [10, 11]. Among these electrode materials, carbon materials are widely used in electric double-layer capacitors (EDLCs), since these materials can provide huge surface area and porous structures to build charges at the electrode/electrolyte interface [12, 13, 14].

Graphene has drawn a lot of interest to be used as an electrode material for EDLCs due to its excellent electrical conductivity, high-rate capability, and electrochemical stability. It has been stated that the graphene nanosheets can provide a maximum capacitance of around 21 μF cm^{-2} (specific capacitance of 550 F g^{-1}) with a specific surface area of 2675 m^2 g^{-1} being fully accessible to the ions [15, 16]. However, it is still difficult to produce perfect 2D graphene structures on a large scale to be used as an electrode material. Alternatively, graphene nanoplatelets (GNPs) comprising generally of around 2-10 layers are made by exfoliating the natural graphite that can be produced in high volume and with low production cost thereby offering a remarkable high surface area with excellent electrical, mechanical, and chemical properties [17]. The bare GNPs as an electrode material without any surface modifications have been reported elsewhere [16, 18, 19]. Functionalization of the surface is one of the key processing strategies to enhance the electrochemical properties of GNPs [20, 21]. The GNPs have also been used along with other materials as a supercapacitor electrode to enhance their electrochemical performance. For instance, Rubaye *et. al* synthesized $MnCo_2O_4$ nanoflakes/graphene nanoplatelets resulting in the capacitance of ~1268 F g^{-1} at a scan rate of 1 mV s^{-1} in 1 M KOH aqueous solution [22]. Ahmed et. al reported fabrication of free-standing and flexible form of PEDOT:PSS/GNP nanocomposite, that delivers a specific capacitance of ~106 F g^{-1} in an Ionic liquid [23].

In addition to GNPs, carbon nanofiber (CNFs) is also one of the important carbon-based one-dimensional materials offering shortened diffusion lengths for ion transport in EDLCs. Other important characteristics of CNFs for supercapacitors are their good stability, high length-to-diameter ratio, good thermal and electrical conductivities, and flexibility [24]. The CNFs have been used as an active material for supercapacitor applications offering good electrochemical properties [25, 26, 27, 28, 29].

Binder-free electrode for supercapacitors is highly desirable for lightweight and flexible energy applications. However, carbon-based supercapacitors include a polymeric binding agent for holding the active materials and conductive fillers together in the electrode. The binder and the conductive filler together make up to 20 % of the overall electrode weight without any contributions to enhancing the specific capacitance of the electrode. In fact, it adversely affects the electrochemical performance of the active materials [30, 31]. There have been some reports on binder-free electrodes based on carbon materials in the literature [32, 33, 14] that used CNTs or graphene as conductive binders. Nevertheless, no reports have been presented as binder-free all-carbon composites as an electrode in supercapacitors. The development of a binder-free all-carbon electrode is significant innovation in the field of energy storage and electrochemistry. Moreover, it offers additional advantageous such as enhancing electrical conductivity, providing mechanical stability, inducing synergistic effects, and promoting sustainability. Additionally, it is also important to understand how the binder-free electrodes perform at different concentrations of an electrolyte. It is widely understood that the type and concentration of electrolyte has a significant effect on the electrochemical performance of supercapacitors. For instance, Yasnur *et al.* investigated the impact of the concentration of potassium hydroxides (KOH) on the electrochemical performance of oxides nanostructures. They observed the specific capacitance increased with increasing the concentration of KOH [34]. Among electrolytes, aqueous electrolytes like KOH are conventionally used due to their low cost, environment friendliness and simplifying the fabrication steps of supercapacitors. In summary, the development of binder-free all-carbon electrodes along with understanding of their performance in different concentrations of electrolyte holds great promise in the field of energy storage and electrochemistry.

Here in this paper, we have fabricated a binder-free all-carbon composite electrodes for supercapacitors. The CNF/ GNP composite with GNPs concentrations ranging from 10 wt. % to 90 wt.% (with the increment of 20 wt.%) was used as symmetric supercapacitor electrodes in an aqueous KOH electrolyte. The electrochemical performance of the CNFs/GNPs was found to be greatly enhanced by increasing the contents of the GNPs in the composite. The electrochemical performance of the composite electrodes was also studied in different molar concentrations of aqueous KOH electrolyte solution. Furthermore, the composite electrode showed a reduced equivalent series resistance (ESR) which is probably due to the absence of a binder and further supported by the formation of percolating network of CNFs in the composite. The overall enhanced electrochemical performance of the composite can be related to the presence of a positive synergistic effect between CNFs and the GNPs.

2. Experimental

2.1. Preparation of the electrodes for supercapacitor

Commercial CNFs were purchased from Grupo Antolin (98.99% purity) with diameters of 20 nm to 80 nm, a specific area of 83 $m^2\ g^{-1,}$ and a resistivity of $10^{-2}\ \Omega.cm$. The GNPs (Grade-C) consisting of 4- 5 layers of graphene with diameters < 2 µm and a specific area of 750 $m^2\ g^{-1}$ were acquired from Aldrich Chemistry (99.999% purity). The CNF/ GNP composite was then prepared by a simple powder processing method. The fabrication process of the composite electrode material involved, ball milling, and mixing the powders in an agate mortar to form a slurry without a binder in contrast to our previous studies where a binder was used [35, 36, 37]. The powder was mixed in 20 ml acetone (99%) to form a slurry and performed ultrasonic (Elmasomic SH 10) for 20 min at 35 ºC. Finally, the slurry of the mixture was dried in an oven at 70 ºC for 60 min. Then the slurry was pressed by using the press and moulding machine (Shimadzu) with a die set (10 mm) at 10 Ton to form the supercapacitor electrode without the binder. The concentration of GNPs used were 10 wt.%, 30 wt.%, 50 wt.%, 70 wt.%, and 90 wt.% in CNF/GNP composite named hereafter as X1, X2, X3, X4, and X5 respectively. We attempted to increase the GNP concentration beyond this ratio, such as making 95 wt.% GNP and 5 wt.% CNF, but the electrodes were found to be mechanically unstable. Similarly, electrodes composed of solely GNP or CNFs, intended for comparison purpose, resulted also in the mechanical instability. Therefore, a 5 wt.% polyvinylidene fluoride (PVDF) was necessary for creating these electrodes compared to successful creation of below 90 wt.% GNP/10 wt.% CNF composite electrodes without binders. The thickness and mass loading of each electrode was 0.57 mm and 0.1 mg cm^{-2}.

2.2. Electrochemical characterization

The electrochemical characterization of the prepared symmetrical supercapacitors was tested in two-electrode Swagelok cells to assemble the components. Potentiostate (PGZ- 402) was used to investigate electrochemical properties by three different methods: cyclic voltammetry (CV) at the scan rate (5 mV s^{-1} to 100 mV s^{-1}), galvanostatic charge/ discharge (GCD) at current density (0.4 A g^{-1} to 1.43 A g^{-1}), and electrochemical impedance spectroscopy (EIS) in the frequency range of (10 kHz to 0.1 Hz).

2.3. Surface and pores characterization

The surface morphology and microstructure of X1 and X5 samples, as well as the content of carbon nanofibers (CNF) and graphene nanoplatelets (GNP), were investigated using a Hitachi SU5000 field-emission scanning electron microscope (FESEM). X-ray diffraction (XRD) analysis was conducted using a Malvern Panalytical Empyrean-3 to determine the macroscopic

crystal structure. XRD was operated in reflection mode at a voltage of 45 kV and a current of 40 mA, utilizing Cu Kα radiation (λ = 1.54 Å). Raman spectra were acquired using a 532 nm laser-based Renishaw inVia Raman spectrometer, employing a 30-second exposure time at 25 mW laser power. The specific surface area (SSA) and the pore size distribution (PSD) of CNFs/ GNPs composite at different concentrations of GNPs were determined by N_2 adsorption/desorption isotherms at 77 *K* by using Brunauer- Emmett- Teller (BET) analyzer (TriStar 3000 V 6. 04A).

3. Results and Discussion

3.1 Characteristics of the composite electrodes

Figure 1a-b shows the SEM images CNF/GNP composite containing the lowest (10 wt.%) and highest (90 wt.%) concentrations of GNPs respectively. The cylindrical shape of CNFs formed a well-connected network structure with the planar form of GNPs. Such network structure forms interconnecting support for each other and hence facilitates the fabrication of the composite electrodes without even the need for using a binding agent. A uniform and homogeneous nanocomposite structure was evident in both samples. Specifically, for X1, a significantly higher abundance of carbon nanofibers (CNFs) was observed compared to graphene nanoplatelets (GNPs). Conversely, in X5, there was a notably higher presence of uniform spherical GNPs compared to fibrous CNFs. This aligns with the composition, where X1 contains only 10 wt% GNPs while X5 comprises 90 wt% GNPs. The uniform nanocomposite with higher conductive GNPs is responsible for the boosted charge transfer kinetics which will be explored in detail in the electrochemical section.

A range of different binder-free compositions of the composite electrode has been fabricated by just varying the weight fraction of GNPs as shown in Figure 1c. The SSA of the composites at different weight fractions of the GNPs were calculated from the adsorption-desorption isotherms as shown in Supplementary Information Figure S1. The effect of GNPs on the SSA of the composite is displayed in Figure 1d. The SSA of the X1, X2, X3, X4, and X5 samples were around 258 $m^2\ g^{-1}$, 271 $m^2\ g^{-1}$, 423 $m^2\ g^{-1}$, 529 $m^2\ g^{-1}$, and 696 $m^2\ g^{-1}$ respectively. Clearly, the SSA of the as-received CNFs (83 $m^2\ g^{-1}$) has been enhanced by the addition of GNPs in the composite. This enhancement in the SSA can be attributed to the presence of porosity in the composite network structure. The type of porosity found in the CNFs/GNPs composite consists of micro-, meso-, and macropores as can be seen from their PSD shown in the Supplementary Information Figure S1.

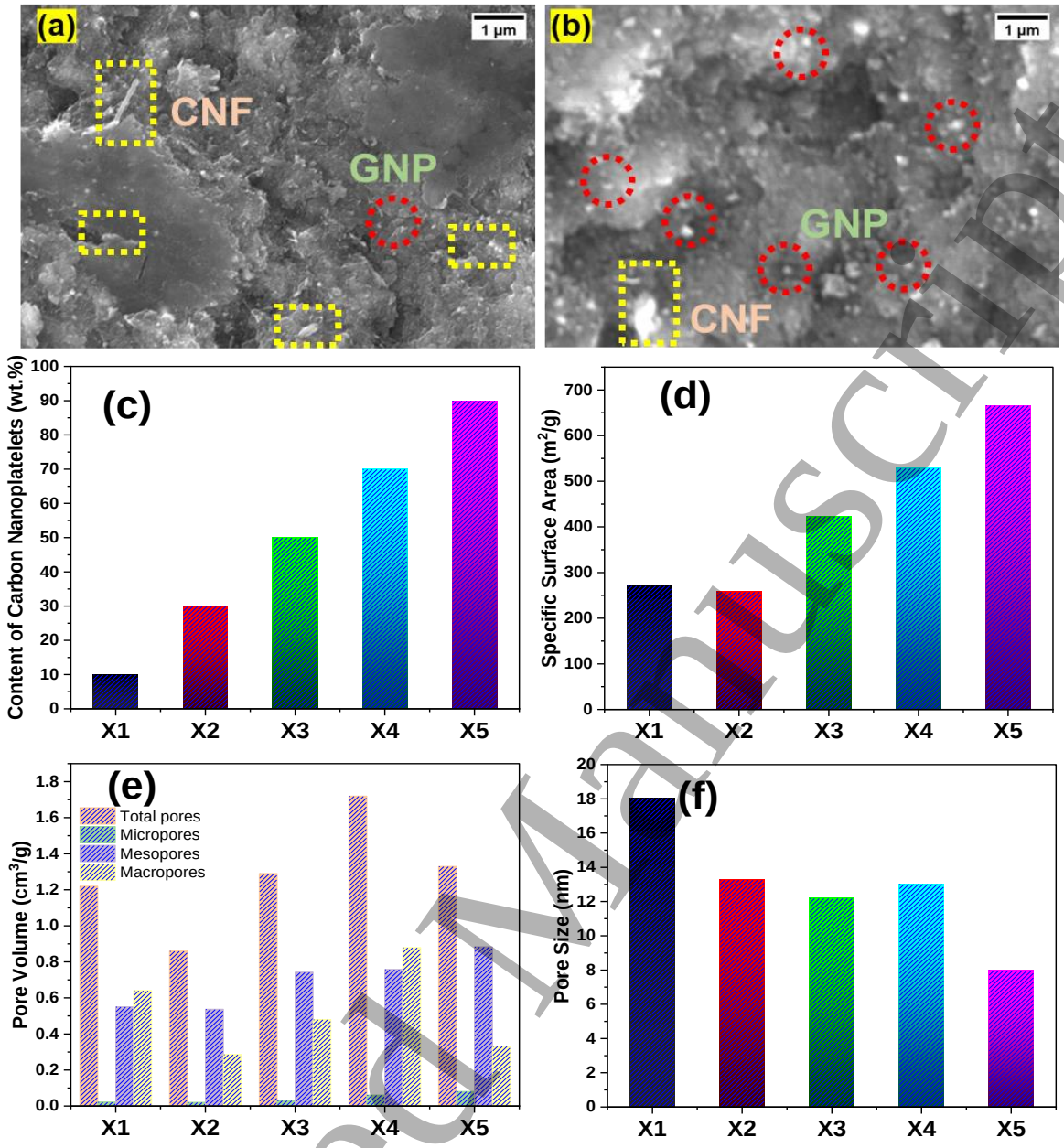

Figure 1: (a-b) Scanning electron microscopy (SEM) images of carbon nanofibers/graphene nanoplatelets (CNFs/GNPs) composite with the concentration of 10 wt.% (X1) and 90 wt% (X5) GNPs respectively, the red dotted circle represents the GNP, and the yellow dotted rectangles highlight the CNF structure. **(c)** The weight fractions of the GNPs in the CNFs/GNPs composite electrodes; (d) The changes in the specific surface area (SSA) of the composites at different weight fractions of GNPs; (e-f) The variations in the pore volume and pore sizes in the composite as a function of varying the weight fractions of the GNPs respectively.

Figure 1e shows the variations in the volume of total pores, micropores, mesopores, and macropores in X1-X5. As can be seen in Figure 1e, the total pore volume is showing an increasing trend for X2-X4 which is due to an increase in the volume of mesopores and macropores. There is a slight increase in the volume of the micropores as well with the increase in the GNP fractions from 10 wt.% to 90 wt.%. The presence of the micropores was estimated from the t-plots as shown in Supplementary Information Figure S1. It is very interesting to note that the pore volume decreased from 1.2 down to 0.8 with increasing GNPs from 10wt.% to 30wt.%. This behavior probably is due to changes in the macropores volume as shown in Figure 1e and possibly also due to the reduction in the pore size (Supplementary Information Figure S1). A similar trend can be seen for the composite when the concentration of the GNP increased from 70 wt.% to 90 wt.% which is because the dominant pores are in the form of macropores rather than meso- or micropores. Furthermore, the effect of the pore size can also contribute to the changes in the total pore volume.

Figure 1f displays the changes in the pore size with the changes in the GNP concentrations. The pore size is reduced from around 18 nm (X1) down to around 8 nm (X5) by increasing the concentration of the GNPs. This probably relates to the closure of the pores due to the dominant planar nature of the GNPs in the composite. Furthermore, the decrease in the pore sizes with increasing the GNPs fractions is responsible for the increase in the SSA. The pore sizes greater than 18 nm were also observed in the composite which is shown in Figure S1. For example, pore sizes of around 112 nm and 162 nm were also noticed in the macroscale region in the case of X2, X3, and X4. The dominant pore sizes in all the samples were found to be around 12 nm and 34 nm as can be seen in Figure S1.

The powder X-ray diffraction (XRD) spectra depicted in Figure 3 show the profiles of X1 and X5. In both samples, two distinct peaks are evident at 25.8° and 28.7°. The peak observed at 25.8° corresponds to the (002) plane of graphene nanoplatelets (GNPs) [38], while the peak centered at 28.7° represents the (111) lattice plane of carbon nanofibers (CNFs) [39]. In X1 samples, both peaks are prominent, whereas in X5, the peak corresponding to CNFs is notably fainter compared to the GNP peak. This discrepancy arises from the lower CNF content in X5 (10 wt%) compared to X1 (90 wt%), resulting in the diminished intensity of the CNF structure peak in X5.

Figure 3 illustrates the Raman spectra obtained from both X1 and X5 samples. Both samples displayed characteristic D, G, and 2D peaks indicative of graphene-like structures. The distinguishing factor between X1 and X5 lies in their I_D/I_G ratio. Specifically, for X1, this ratio was measured at 0.7, whereas for X5, it was determined to be 0.53. The lower I_D/I_G ratio

observed in X5 indicates a nanocomposite with fewer defects and a higher graphene content. Consequently, this graphene-based structure with reduced defects exhibits enhanced electrical conductivity, facilitating rapid charge transfer.

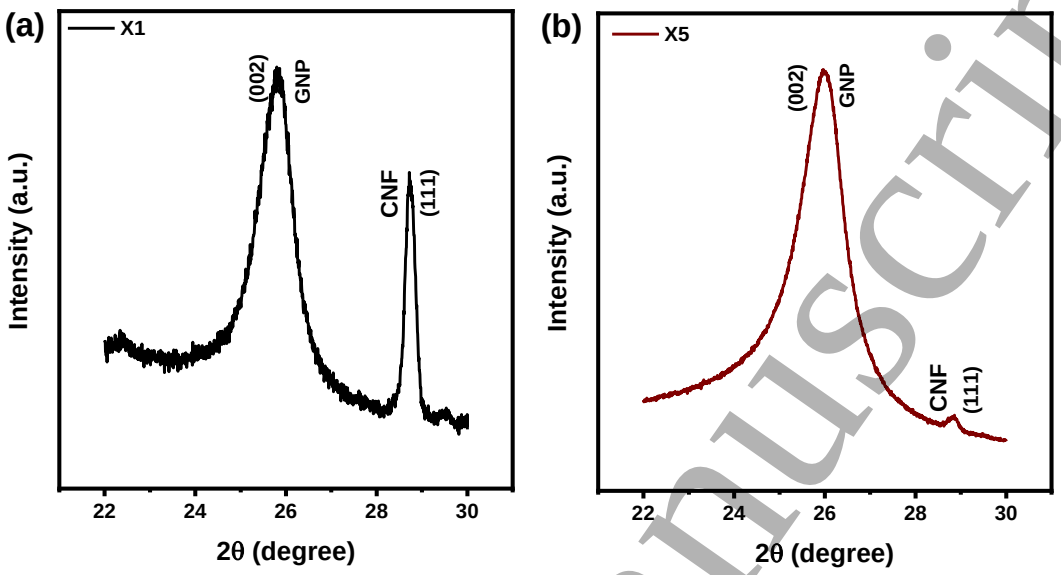

Figure 2: XRD spectra of (a) X1(CNFs: 90%, GNP: 10%), and (b) X5 (CNFs: 10%, GNPs: 90%).

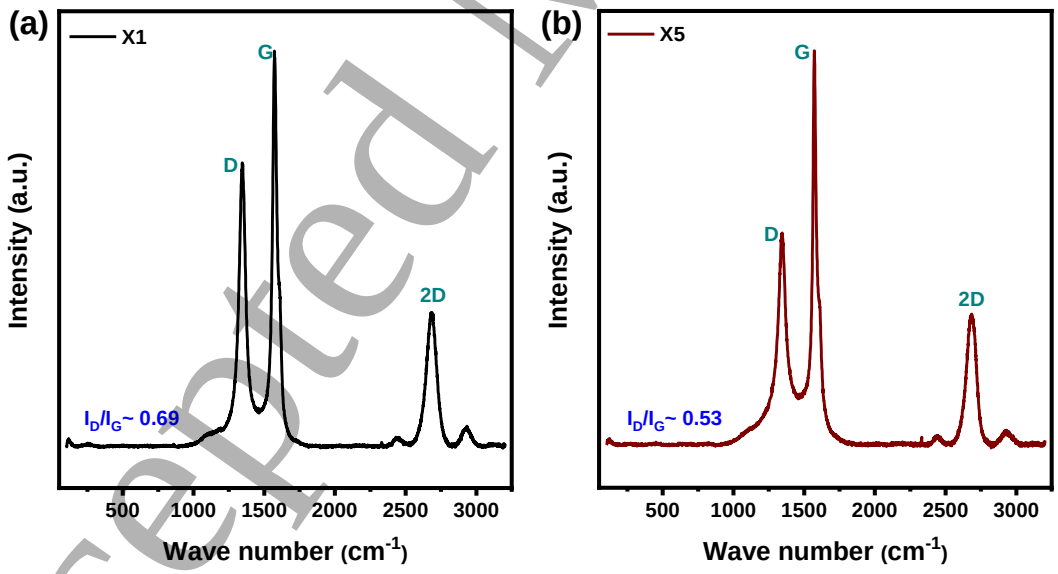

Figure 3: Raman spectra of (a) X1(CNFs: 90%, GNP: 10%), and (b) X5 (CNFs: 10%, GNPs: 90%).

3.2 Electrochemical performance of the composite electrodes:

Cyclic voltammetry is a typical technique that is used to estimate the capacitance of the electrode materials. Figure 4a shows CV curves of X1-X5, CNFs, and GNPs at a scan rate of 5 mV s^{-1}. The rectangular nature of the CV curves in our samples reflects an ideal capacitive behavior. With increasing the scan rate, the rectangular shape of the curves are distorted in shape which is caused by the ohmic resistance and due to the slow ion diffusion kinetics (see Figure S3) as reported elsewhere [40].

The region under the CV curve determines the total charge stored in the supercapacitor. Figure 4b shows a comparison of the changes in the specific capacitances of the samples with increasing the scan rates from 5 mV s^{-1} to 100 mV s^{-1}. The specific capacitances at different scan rates were estimated using the equations (1 & 2) provided in the Supplementary Information. The C_s of CNFs, GNPs, X1, X2, X3, X4, and X5 at 5 mV $s^{-1}$are estimated to be around 23 F g^{-1}, 33 F g^{-1}, 47 F g^{-1}, 75 F g^{-1}, 89 F g^{-1}, 102 F g^{-1}, and 120 F g^{-1} respectively.

The C_s of the CNFs is increased with increasing the concentrations of the GNPs. The increase in the specific capacitance of the composites is probably due to the increase in the SSA and decrease in the pore sizes as discussed earlier. Furthermore, enhanced connectivity of the high surface area of GNPs with highly conductive CNFs can also contribute to the enhancement in the specific capacitances of the composite. The gradual decrease in capacitance with an increase in scan rate from 5 mV s^{-1} to 100 mV s^{-1} for CNFs, GNP, X1, X2, X3, X4, and X5 are around 48, 79, 45, 53, 60, 72 % respectively. At a high scan rate, the ions have a short time to penetrate the inner porous structure of the electrode to form a double layer, therefor the capacitance is likely from the contributions from the outer surfaces of the electrode.

A comparison between the specific capacitances of carbon-carbon composite electrodes fabricated by different methods and tested in various electrolytes is presented in Table 1. For instance, Murugan et al., fabricated the mesoporous carbon-based composite with waste plastic-derived graphene using PVDF as a binder [41]. The composite electrode delivers a capacitance of 18.6 F g^{-1} at a current density of 0.05 A g^{-1} in a 6 M KOH electrolyte solution. Fikry et al., constructed the graphene/carbon nanotube composite employing Polyurethane as a binder [42]. The graphene/CNT composite presented the specific capacitance of 179 F g^{-1} at a scan rate of 10 mV s^{-1} (in 1M NaCl electrolyte). Abdul Hakim et al., study showed that activated carbon and graphene nanoplatelets composite bonded using PTFE delivers a capacitance of 98.3 F g^{-1} at a discharge current of 4 mA (in 6M KOH electrolyte) [43]. Cheng et al., reported the composite fabrication based on multidimensional carbon materials including carbon black (CB), carbon nanofibers (CNFs), reduced Graphene oxide (RGO), and Activated

carbon (AC) using aqueous binder solution containing carboxymethyl cellulose sodium (CMC) and styrene butadiene rubber (SBR) [45]. The composite displays a capacitance of 106 F g^{-1} at a current density of 0.5 A g^{-1} in [1 M tetraethylammonium tetrafluoroborate (TEA-BF4)/acetonitrile (ACN)] electrolyte. From these studies, it is evident that our all-carbon binder-free composite electrodes have a high potential to be used as supercapacitors.

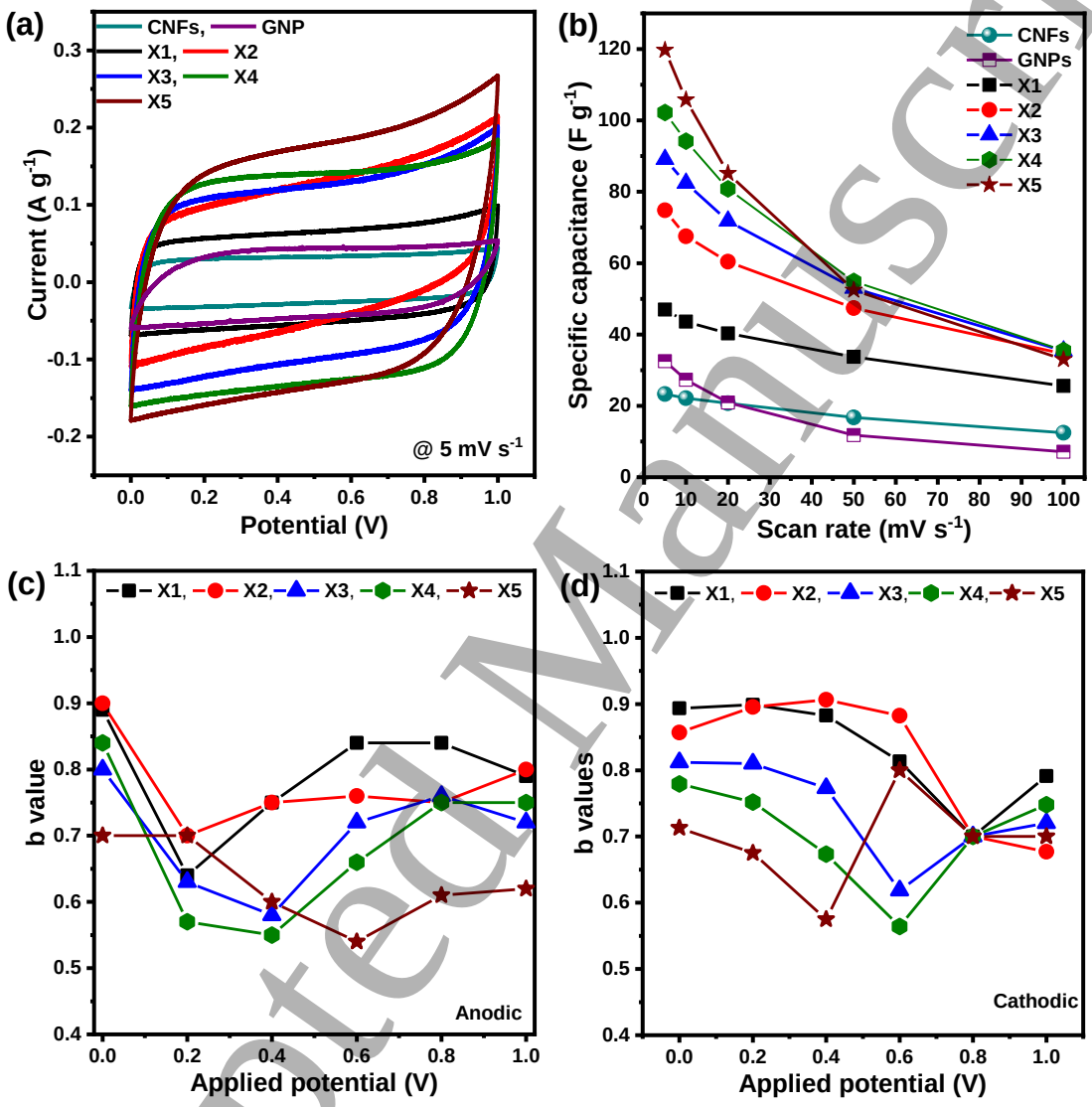

Figure 4: (a) Cyclic Voltammetry comparison at 5 mV s^{-1} for CNFs, GNPs, X1(CNFs: 90%, GNP: 10%), X2 (CNFs: 70%, GNPs: 30%), X3 (CNFs: 50%, GNPs: 50%), X4 (CNFs: 30%, GNPs: 70%) and X5 (CNFs: 10%, GNPs: 90%); **(b)** Variation of specific capacitance with increasing scan rate from 5 mV s^{-1} to 100 mV s^{-1} for CNFs, GNPs and for X1-X5 samples; (**c, d**) Dependence of slope "b" (derived from the linear fitting of log i vs log ν) as a function of cell potential.

Table 1: Specific capacitance comparison between carbon-carbon composites.

Composite	Binder	Electrolyte	Specific Capacitance ($F\ g^{-1}$)		Reference
			Scan rate	Current density	
Graphene/mesoporous carbon	PVDF	6 M KOH		18.6 F g^{-1} at 0.05 A g^{-1}	[41]
Graphene/CNT	Polyurethane	1 M NaCl	179 F g^{-1} at 10 mV s^{-1}		[42]
Graphene nanoplatelets/AC	PTFE	6 M KOH		98.3 F g^{-1} at 4 mA	[43]
AC/Graphene	PTFE	6 M KOH		205 F g^{-1} at 2 A g^{-1}	[44]
AC/CNFs	PVDF	6 M KOH	207 F g^{-1} at 5 mV s^{-1}	130 F g^{-1} at 0.5 A g^{-1}	[35]
AC/CB/RGO/CNFs	CMC/ SBR	TEA-BF4)/ ACN		106 F g^{-1} at 0.5 A g^{-1}	[45]
Graphene/CNTs	No binder	1 M KCl	290 F g^{-1} at 10 mV s^{-1}		[32]
Graphene/Carbon black	No Binder	1.5 M TEMA-TFB/ACN		37.2 F g^{-1} at 0.5 A g^{-1}	[46]
CNFs/GNPs	No Binder	6 M KOH	189 F g^{-1} at 5 mV s^{-1}	142 F g^{-1} at 0.42 A g^{-1}	Current work

The total stored charge in an electrode is a combination of both capacitive and diffusion processes [47]. The capacitive component originates from the ion adsorption/desorption at the electrode-electrolyte interface and very fast faradic reactions. On the other hand, mass transfer kinetics, and ion migration intercalations are responsible for the diffusion phenomena. This charge storage mechanism can be estimated, and both components can be separated by analyzing the CV curves at different scan rates using the power law relation [48].

$$i = av^b \quad (1)$$

where 'i' is the current at a fixed potential for different scan rates, 'ν' is the scan rate, and 'a' and 'b' are the variable parameters. When 'b' tends to 1, the current primarily originates from the capacitive contribution whereas when 'b' is closer to 0.5 implies a diffusion-controlled current response. This method is particularly useful to map the nature of charge storage kinetics at different potentials [49]. To evaluate the b values, log i vs log v was plotted at different applied potentials and the data was fitted linearly. The slope of the fitted line is the measure of the "b" value. The plot and the subsequent fitting are represented in Figure S4. The value of 'b' was calculated for different potentials in both the anodic and cathodic conditions which are then plotted against the applied potential as shown in Figure 4c-d. The value of b ranges from 0.5-0.9 confirming the charge storage mechanism to be mainly dominated by the surface-driven capacitive components. The high surface area of the composite and a better formation of the

electrical double layer at the electrode/electrolyte interface were correlated with the capacitive nature of the charge storage kinetics.

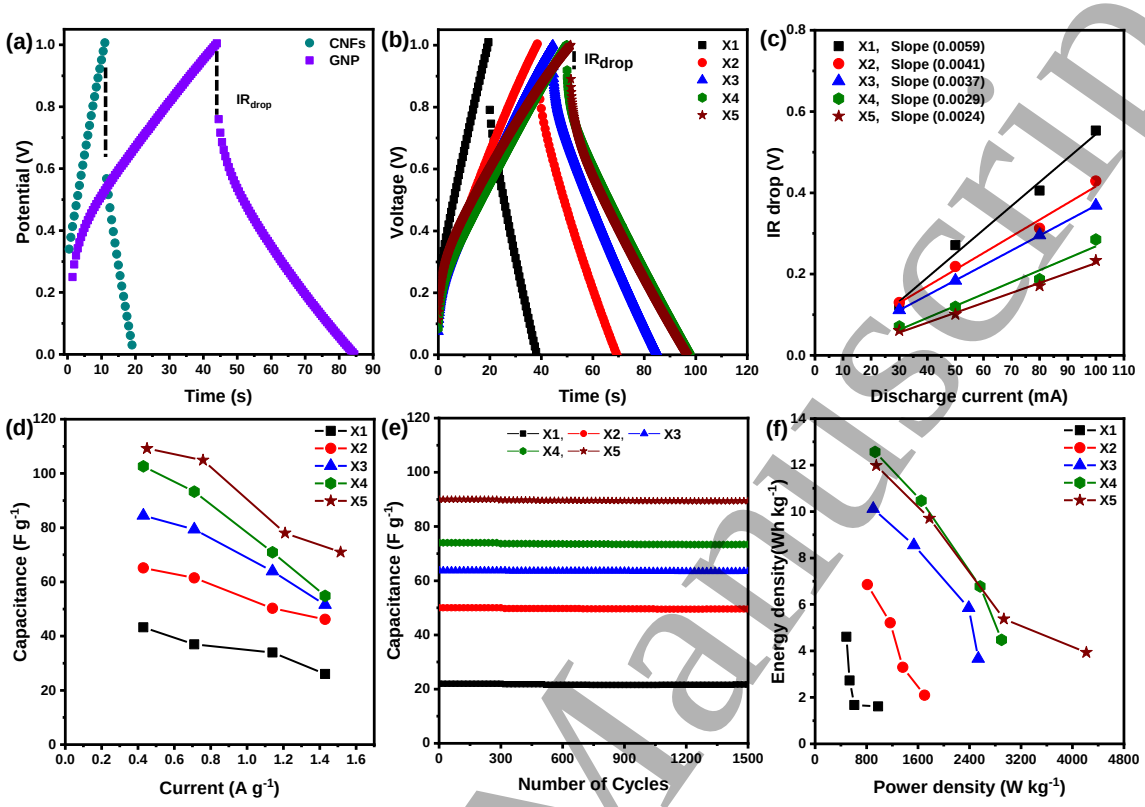

Figure 5: (a-b) The voltage versus time curves obtained from the galvanostatic charge-discharge measurements for CNFs & GNPs, CNFs/GNPs (GNPs:10 wt.%-90 wt.%) respectively; **(c)** the variations in the IR drop versus the discharge currents; **(d)** specific capacitances of the CNFs/GNPs composites versus the discharge current densities; **(e)** capacity retention versus charge-discharge cycles at 1.43 A g^{-1}; **(f)** Ragone plots of the supercapacitors containing different weight fractions of GNPs in the composite electrodes.

The galvanostatic charge-discharge measurements were carried out to understand the voltage-time relationships in CNFs/GNPs composites. Figure 5a-b shows the charge-discharge curves of only CNFs and GNPs, and CNFs/GNPs composites at 0.42 A g^{-1} respectively. The charge-discharge curves show V-shaped symmetrical behavior confirming the electrical double-layer charge storage mechanism in all samples and their remarkable electrochemical reversibility. Furthermore, the CNFs/GNPs show lower IR drop compared to the CNFs and GNPs alone which is possibly because of the binding agent present. The IR drop just after the charging process is due to the equivalent series resistance (ESR) which is also an indication of the

internal resistance of the supercapacitor [50]. The IR drop is enhanced with the increase in the current density for all the samples as shown in an example in Figure S5.

Figure 5c shows a graph between the IR drop versus the discharge currents for X1-X5 supercapacitors. The slope of the plots in Figure 3c at different currents can be used to estimate the overall resistance of the supercapacitor. The smaller the slope, the smaller the overall resistance of the supercapacitor [51]. The value of the slope decreases with increasing the fraction of GNPs in the composite electrodes of the supercapacitors. The ion migration resistance and electrolyte resistances are identical due to the electrolyte (i.e. 1 M KOH) used in the supercapacitors. In our case, the slope is directly related to the electrode resistance. It can be proposed that the higher weight fractions of GNPs (alternatively lower weight fractions of CNFs) and binder-free composite electrodes can essentially decrease the resistance of the supercapacitor and hence enhance their electrochemical performance.

Figure 5d shows the specific capacitances of the composites estimated at different current densities using equation (3) given in the Supplementary Information. The C_s of all the composites decreased with increasing the current density from 0.4 to 1.43 A g^{-1}. Such a decrease in the C_s as a function of increasing current density is probably due to the limited diffusion of electrolyte ions in the microspores which is a well-known phenomenon in supercapacitors. The maximum C_s of around 110 F g^{-1} (at 0.4 A g^{-1}) was achieved for the X5 supercapacitor. The higher concentration of GNPs in the composite significantly enhanced the C_s of the supercapacitor because of their high surface area and reduced pore size as discussed earlier. The charge-discharge cycling stability of up to 1500 cycles at a constant current density of 1.43 A g^{-1} was tested for the supercapacitors. There is no change in the C_s with increasing the charge-discharge cycles as can be seen in Figure 5e. Such stability and high-capacity retention is very desirable criteria for commercial mini-supercapacitor applications.

The energy and power densities of supercapacitors are also the major parameters to consider when evaluating their electrochemical performance in real-world applications. The energy and power densities of the supercapacitors were calculated using equations (4) and (5) as provided in the Supplementary Information. Figure 5f shows the Ragone plots (energy versus power density on a logarithmic scale) of the X1-X5 supercapacitors. Our X4 and X5 supercapacitors exhibited energy densities of 12.6 W h Kg^{-1} and 12 W h Kg^{-1} whereas their maximum power densities were found to be around 2898 W Kg^{-1} and 4216 W Kg^{-1} respectively. On the other hand, the maximum energy and power densities followed a decreasing linear trend with the decrement in the concentration of GNPs. Particularly, the energy density of the X1 supercapacitor sharply decreases from around 4.6 W h Kg^{-1} to 0.16 W h Kg^{-1} when the power

density increases from 486 W Kg^{-1} to 612 W Kg^{-1} and hence reflecting the poor performance of this supercapacitor due to the low concentration of GNPs.

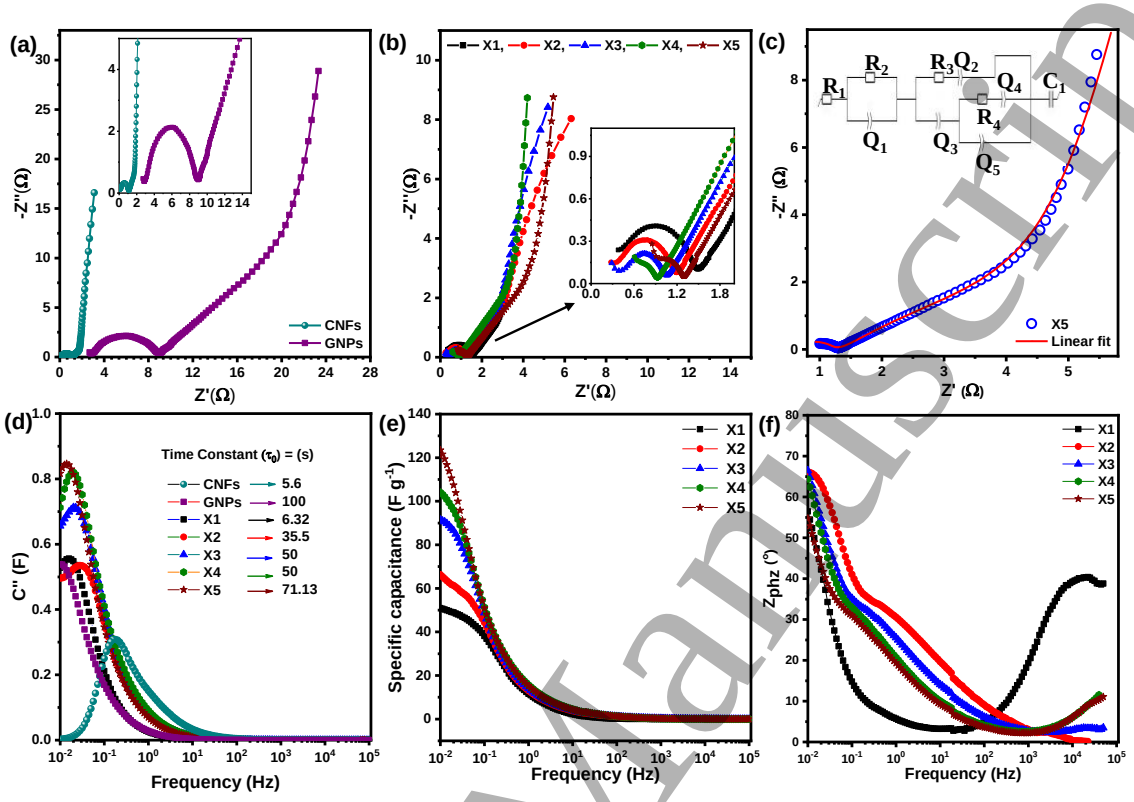

Figure 6: Electrochemical impedance analysis for CNFs, GNPs, X1(CNFs: 90%, GNP: 10%), X2(CNFs: 70%, GNPs: 30%), X3(CNFs: 50%, GNPs: 50%), X4(CNFs: 30%, GNPs: 70%), X5(CNFs: 10%, GNPs: 90%): **(a, b)** Nyquist plots, **(c)** Nyquist plots for X5 and the corresponding fitting using a model equivalent circuit. The inset represents the circuit diagram for the fitted model, **(d)** Imaginary capacitance (C'') at different frequencies; **(e)** The variations in the specific capacitances as a function of the frequency; (f) The relation of phz angle vs frequency.

The charge-transport kinetics of the supercapacitors were further characterized by carrying out the electrochemical impedance spectroscopy (EIS) measurements. Figure 6a-b shows the Nyquist plots corresponding to CNFs and GNPs, and the composites (X1-X5) respectively. The x-axis intercept at the high frequency represents the combined resistance (R_s) comprising of ionic resistance of the electrolyte solution, inherent resistance of electrode materials, and the

contact resistance between the electrode and current collector. The semi-circle loop indicates the electrode conductivity and charge transfer resistance of the electrode materials (R_{ct}) [52]. The formation of the Warburg region from mid to low frequencies is due to the result of the ions penetrating the electrode pores thereby exhibiting both resistive and capacitive characteristics in the supercapacitor. The vertical line at low frequencies represents the capacitive behavior of the supercapacitor. The R_s values for CNFs, GNPs, X1, X2, X3, X4, and X5 are around 0.1 Ω, 2.7 Ω, 0.37 Ω, 0.27 Ω, 0.28 Ω, 0.6 Ω, and 0.8 Ω respectively. The R_s values of the CNFs and X1-X5 supercapacitors are much lower than the GNPs supercapacitor (i.e., 2.7 Ω). The increase in the concentration of GNPs results in the increase in the R_s values of the CNFs/GNPs composite supercapacitor. Even the highest concentration of GNP in the composite (i.e., 90 wt.%) shows smaller R_s compared to GNP which may also be due to the absence of the binding agent. The comparison here may not be ideal with the GNP or CNF supercapacitors because they included the binding agent. It was highly challenging to process and fabricate the binder-free GNP or CNF supercapacitors. Yet, it can somehow give an idea about the role of the binding agents in supercapacitors.

The diameter of the semi-circular region can be utilized to estimate the values of R_{ct}. In our case, the values for CNFs, GNPs, X1, X2, X3, X4, and X5 are around 1 Ω, 6.26 Ω, 1.11 Ω, 0.92 Ω, 0.76 Ω, 0.32 Ω and 0.49 Ω respectively. The much lower R_{ct} values for X4 and X5 supercapacitors in comparison to other samples are because of the homogeneous mixing of CNFs and GNPs powder and due to the absence of insulating biner materials in the composite. The steep slopes at low frequencies in X5 and that CNFs are well dispersed and tethered to GNP particles, help to promote ionic diffusion into GNP pores.

The EIS data was further fitted using a model equivalent circuit for all the samples as shown in an inset of Figure 6c. The first impedance (R_1) stands for the series resistance consisting of contact and solution resistance. The second part of the circuit is expressed by a parallel combination of resistance (R_2), which is a combination of interfacial and leakage resistance, and a constant phase element (Q_1) expressing the mass capacitance. This region signifies the presence of the interfacial layer.

The constant phase element (CPE) emerges due to the nonlinearity and inhomogeneity in the system [53]. The CPE is represented as:

$$Z = Y_0 (j\omega)^{-\alpha} \quad (2)$$

where α is the exponent of CPE and ω is the angular frequency. For α = 0 and α = 1, the component is purely resistive and purely capacitive respectively.

The third region denotes two modified Randle's circuits comprising of a charge transfer resistance (R_3) and two constant phase elements (Q_2 and Q_3) expressing double layer and diffusion components respectively. The entire third region demonstrates the charge transfer kinetics. The presence of two Randle's circuits denotes the presence of two types of materials in the system (CNFs and GNPs). The Values of all the fitted parameters for the composite electrodes are represented in Supplementary Table S1. As the electrodes are made up of a composite, the parallel combination of Randle's circuit was employed. It is to be mentioned that for the pristine CNFs and GNPs the second Randle's circuit was absent (Supplementary S6), which also justifies the suitability of the model. The last part consists of capacitance known as the limit capacitance. The EIS fitting for the X5 sample is represented in Figure 4c. The fitted circuit parameters are tabulated in Table S2. The charge transfer resistance (R_3) of X5 was evaluated to be 0.41 Ω, which is the lowest among other samples and hence manifests a better charge transfer kinetics improving the electrical conductivity and charge storage capability. The values of α in the charge transfer domain (third region) in the case of the X5 sample are > 0.8 which also exhibited that the charge storage is mostly capacitive.

The imaginary capacitance (C'') was calculated using equation (6), as provided in the Supplementary Information (SI), and the time constant is estimated by plotting the graph between imaginary capacitance and frequency which is shown in Figure 6d. The time constant divides the resistive and capacitive regions of supercapacitor behavior, which can be determined by taking the reciprocal of the maximum frequency f_0 as ($\tau_0 = {}^{1}/_{f_0}$). In general, a low value of the time constant is considered a better performance indicator of the supercapacitor in delivering high power in a short time. The time constant for CNFs, GNPs, X1, X2, X3, X4, and X5 is 5.6 s, 100 s, 6.32 s, 35.5 s, 50 s, 50 s, and 70 s respectively. The time constant is influenced by several factors, including the electrolyte, the conductivity, and the thickness of the electrode [54]. Since the electrolyte and the thickness of the electrodes are similar for all the supercapacitors, hence time constant affects only the conductivity of the electrode materials. The increase in time constant also reveals the increase in energy density as can be seen from the Ragone plots as shown in Figure 5f.

The C_s of all the supercapacitors were also estimated from the impedance measurements using equation (7) provided in the Supplementary Information. The changes in the C_s as a function of frequency is shown in Figure 6e. As the frequency value decreases, the permittivity increases so the electric field decreases. Therefore, the concentration of ions becomes lower near the electrode surface. However, the ions have enough time to penetrate deeply into the pores, so

the capacitance value increases. Moreover, the number of ions that participate in the charging process becomes larger with increasing GNPs concentration. Therefore, the C_s is increased with increasing the concentrations of GNPs exhibiting a maximum capacitance of around 123 F g^{-1} for X5 supercapacitor at very low frequency (0.01 Hz). The C_s as shown in Figure 6e fully support the C_s obtained from the CV measurements at different scan rates as discussed earlier in Figure 4. Figure 6(f) represents the variation of phase angle as a function of frequency, which is known as Bode plot. The phase angles at low frequency 0.01 Hz for X1, X2, X3, X4, and X5 is 57°, 66°, 67°, 64° and 55° respectively. These values are close to 90° which means better capacitive performance and rapid charge discharge process.

The variation of C_s and the SSA as a function of the volume fraction of GNPs is shown in Figures 7a-b. The weight fraction of the GNPs in the composite is converted into the volume fractions for enhancing clarity in the representation of the data and it is conventionally being used in mathematical expressions like the rule of mixtures [55]. The rule of the mixture is normally used to characterize the properties of the material and for the presence of synergism in the composite [56]. The experimental results should always be considered as the rule of the mixture is based on several assumptions and ignores any effect arising due to the interactions between the components of the composites. Both the C_s and the SSA of the composite in Figure 7a-b show an increasing trend with increasing the volume fraction of GNPs. Such increasing trends in specific capacitances and specific surface areas follow a similar increasing trend obtained from the rule of mixture. But the results obtained experimentally are greater than what is obtained from the rule of the mixture and hence show a positive effect C_s and the SSA as shown in Figure 7a-b. The deviation in the experimental and theoretical results is justified as the rule of the mixture just simply does not take into account the interfacial strengthening of the fibers and the matrix in a composite. Hence, the presence of the positive synergistic effect is probably due to the formation of conducting pathways or enhanced interactions between CNFs and GNPs which may also be further supported by the absence of a nonconductive binder in the composites.

The understanding of the conducting network formation in composites (particularly in conductive filler/insulating matrix composites) is commonly understood by determining the percolation threshold [57, 58, 59]. The percolation threshold (V_{fc}) is the critical volume fraction where the conducting network is formed and the graph between the resistance and the volume fraction follows an S-shaped characteristic behavior indicating three regions such as conducting, percolating, and insulating [60].

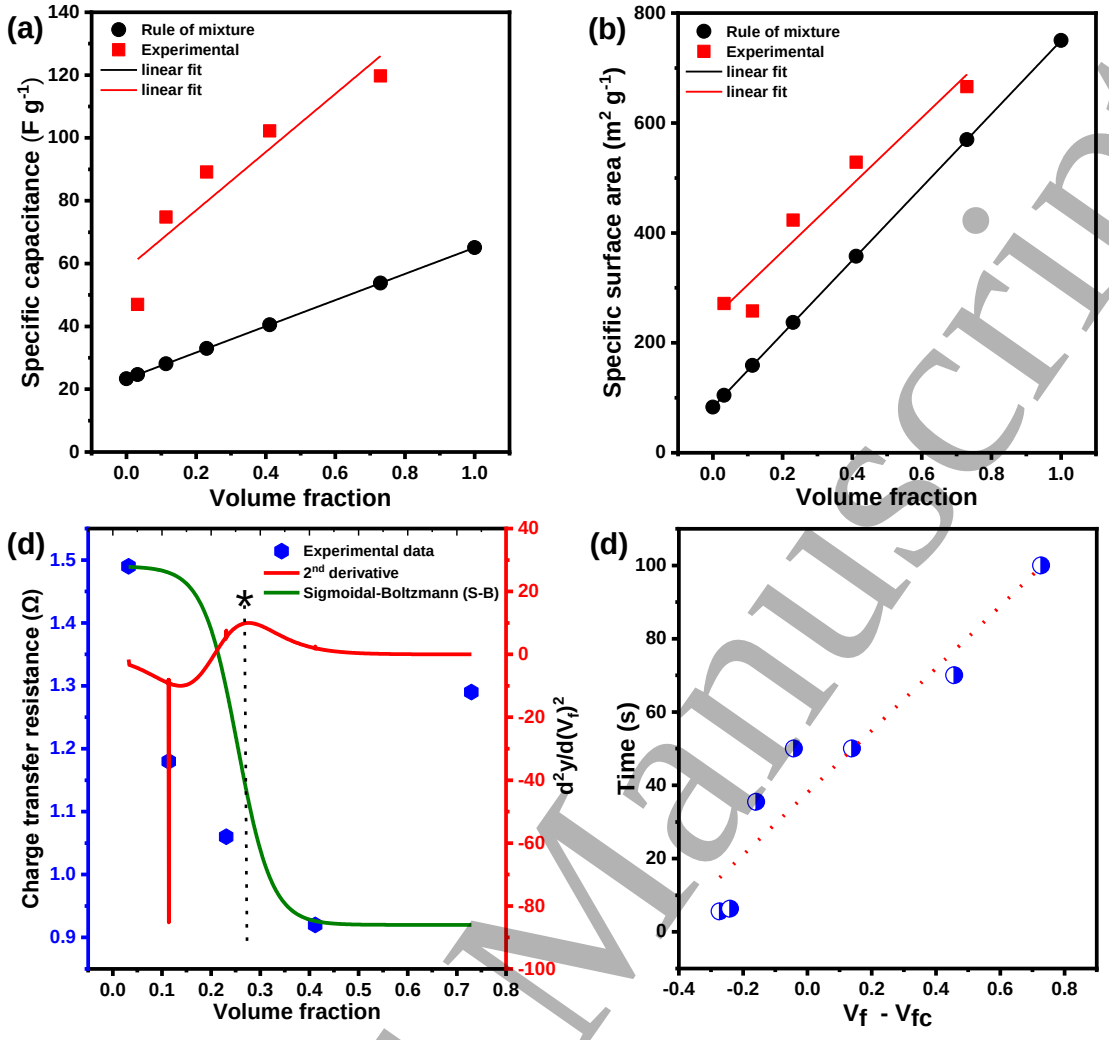

Figure 7: (a-b) Specific capacitances and specific surface area, experimental and theoretical, of the carbon nanofiber/graphene nanoplatelets (CNFs/GNPs) composites are plotted as a function of volume fraction respectively; **(c)** Charge transfer resistance (R_{ct}) of electrode versus volume fraction exhibiting S-shaped Sigmodal-Boltzmann (S-B) behavior resulting in the threshold limit (highlighted as *) of around 0.273 as derived from the maximum of the 2nd derivative of the S-B fit; **(d)** plot of time (sec) versus volume fraction with the linear fit yielding a positive slope of 85 sec.

Figure 7c shows the plot of the resistance of the composite electrode versus the volume fraction of GNPs in the composite. Following a partial fitting by Sigmoidal-Boltzmann, an S-shaped characteristic can be seen. The second-derivative results in the maximum peak corresponding to the V_{fc} around 0.273. The conductive network formation is affected by the volume fraction

of the GNPs. At a very high GNPs concentration, the graph suggests the opposite of the expected results from the percolation theory. At around 90 wt.% GNPs, the behavior of the graph suggests less conductivity in the composite opposite to the percolation theory. It makes sense as the GNPs are not an entirely insulating material like the polymers used to study the percolation theory. Furthermore, the maximum specific capacitance also doesn't lie at the percolation threshold as has been reported for other materials in the literature [59]. The X5 sample shows the highest specific capacitance for the highest volume fraction of GNPs. This means a very low concentration of CNFs is sufficient to create conducting networks in the composite structure of the electrodes thereby increasing an enhanced electrochemical performance. Figure 7d shows the plot of the relaxation time versus the V_f -V_{fc}. The fit line in Figure 7d results in a positive slope of around 85 sec. The power delivery of the composite electrode is reduced at the expense of increased charge storage (C_s). Hence, tuning of the desired level of power delivery and energy storage can be achieved by varying the GNP concentrations in the GNFs/GNPs composite supercapacitor electrodes.

Understanding the effect of electrolyte concentration on the electrochemical performance of the composite electrodes is also very important for desirable outputs from the supercapacitors. Tuning the electrochemical performance can also be achieved by varying the concentration of the electrolyte. The concentration of 1 M KOH is increased to 6 M KOH for the best performing sample i.e. X5. As discussed earlier, the performance of the X5 sample was found to be excellent compared to other samples tested in 1 M KOH. The X5 sample is also tested in 6 M KOH solution, and the obtained electrochemical results are shown in Figure 6 and the Supplementary Information Figure S7. The 6 M KOH electrolyte in the X5(CNFs: 10 wt%, GNP: 90 wt%) supercapacitors induce faster current response without any deviation in the cyclic voltammogram shape and displaying a wider area under the curve at a scan rate of 5 mV s^{-1} (as compared to the supercapacitor tested with 1M KOH electrolyte) as shown in Figure 8a. The C_s, as estimated from CV (Figure 8a and Figure S7), in 6 M KOH were increased to around 189 F g^{-1} compared to 120 F g^{-1} obtained in 1 M KOH at the scan rate of 5 mV s^{-1}. The C_s in 6 M KOH decreased with increasing the scan rate but were still higher than the C_s in 1 M KOH as shown in the inset bar chart diagram of Figure 6a.

The C_s capacitances in 6 M KOH were also estimated from the charge-discharge curves shown in Figure 8b and the Supplementary Information Figure S8. The charge/discharge profiles of X5 at current densities from 0.16 to 1.43 A g^{-1} in 6 M KOH show symmetrical behavior with lower potential drop at the reverse of the current and longer charge and discharge times in comparison to testing in 1 M KOH as shown in Figure S8 and Figure 8b. The C_s at 0.16 A g^{-1}

and 1.43 A g^{-1} are around 142 F g^{-1} and 108 F g^{-1} in 6 M KOH respectively which are higher in comparison to 1 M KOH as shown in Figure 8b.

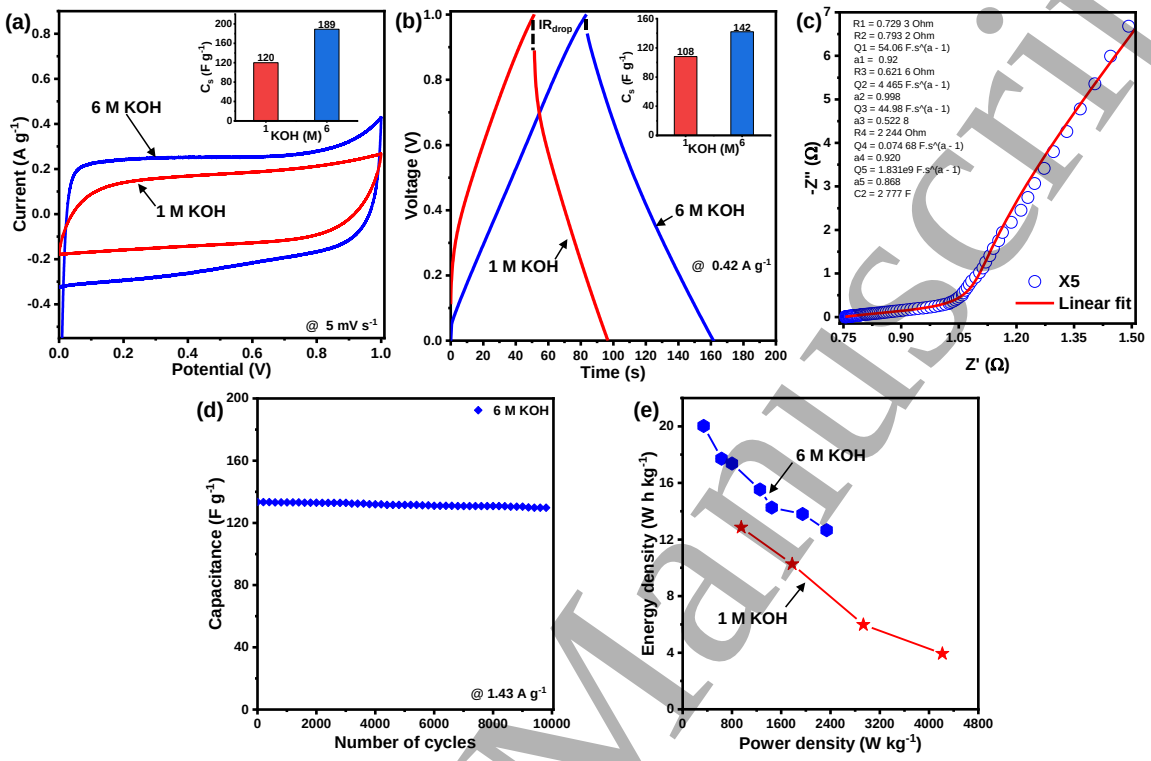

Figure 8: (a) Cyclic voltammograms at 5 mV s^{-1} and the specific capacitances (inset) of X5 (CNFs: 10 wt%, GNP: 90 wt%) composite electrodes tested in 1 M KOH and 6 M KOH are plotted as a function of increasing scan rates from 5 mVs^{-1} to 200 mV s^{-1}; **(b)** charge-discharge curves at 0.42 A g^{-1} and the changes in the specific capacitances as a function of current densities; **(c)** Charge discharge cyclic stability at 1.43 A g^{-1};**(d)** Ragone plot of X5 sample in 1 M KOH and 6 M KOH;**(e)** Nyquist plots for X5 in 6 M KOH electrolyte and the corresponding fitting using the same model equivalent circuit shown in the inset of Fig. 4c.

The long-term charge/discharge cycling stability up to 10000 cycles at a constant current density of 1.43 A g^{-1} reveals a high retention in the specific capacitance as can be seen in Figure 8c. The increase in the capacitance values with an increase in the concentration of KOH can be explained by the fact that the conductivity of an electrolyte increases generally with its concentration in an aqueous solution. Thus, 6 M KOH will provide higher conductivity with high chances of OH^- ions being accessible to the electrode surface than in 1 M KOH solution thereby enhancing charge transfer in both bulk electrolyte and electrode [61].

The Ragone plot in Figure 8d demonstrates the X5 EDLC in 6M KOH delivers a high energy density of 20 W h kg^{-1} with the corresponding power density of 340 W kg^{-1}. Similarly, the lowest energy density of 12.66 W h kg^{-1} corresponds to the highest power density of 2336 W kg^{-1} for the X5 EDLC in 6 M KOH. Figure 8e shows the EIS curve displaying the R_s value of X5 in 6 M KOH of around 0.75 Ω which is lower than in 1 M KOH. The apparent non-existence of any semi-circular region confirms the presence of better charge transfer kinetics in the composite electrode. The impedance spectra are further fitted using the same model equivalent circuit which was utilized for the analysis of the supercapacitor in 1 M KOH electrolyte. The higher KOH concentration is found to enhance the charge transfer kinetics resulting in a significant decrease of equivalent resistances (Supplementary Table S2). From Table S2, it is also quite evident that the increase in electrolyte concentration also plays a significant role in the improvement of all the capacitive components and matches with the results obtained by the cyclic voltammetry and the charging/ discharging analysis. EIS was also conducted before and after extended cycles to examine the dynamics of current response and alterations in internal resistance throughout the charge-discharge process. Subsequent EIS measurements after 10000 charge-discharge cycles (as shown in SI Figure 9) exhibited no substantial changes in ESR values, demonstrating the exceptional stability of the supercapacitor device.

The increase in capacitance with an increase in electrolyte concentration could be related to the following aspects. (1) the conductivity of an electrolyte can significantly impact the performance of a supercapacitor. In literature, it has been stated that the specific conductivity of KOH rises as its concentration increases, peaking around 6 M; however, beyond this point, conductivity starts to decline gradually. We have found as shown in Figure 6a, with the increase in the concentration of KOH, the shape of the CNF/GNPs composite electrode becomes more symmetric, rectangular, and larger in area. A similar trend was observed by Krishnan et al., for the RGO/Carbon black composite electrodes with an increased concentration from 1.5 to 6 M KOH [62]. (2), the improvement of charge transfer kinetics with an increase in KOH concentration as can be seen from the EIS measurements in Figures 4b and 6e.

4. Conclusions

An all-carbon binder-free composite (CNFs/GNPs) electrode with enhanced electrochemical properties in aqueous electrolytes (1M and 6M KOH) was successfully fabricated using a powder processing method. The cylindrical CNFs formed a well-connected network with the GNPs with porous morphology dominating as a mesoporous structure. The SSA of the composites was increased while the pore sizes were decreased as a function of increasing the

concentrations of GNPs. The maximum specific capacitance of 120 F g^{-1} was achieved for CNFs/GNPs (90wt.%GNP) which is greater than the pristine CNFs in 1 M KOH and is further increased to 189 F g^{-1} in 6 M KOH. The composite electrodes presented a long-term charge/discharge reversibility. The best-performing supercapacitor electrodes among the given compositions delivered the maximum power density of 4200 W kg^{-1} at 0.42 A g^{-1} in 1 M KOH and the maximum energy density of around 20 W h kg^{-1} at 0.16 A g^{-1} in 6 M KOH. The detailed electrochemical characterization (e.g., power law, EIS) manifests the evolution of the charge storage mechanism in CNFs/GNPs composites is mainly due to charge storage as a double layer. The overall improved electrochemical performance of the composite is because of the presence of a positive synergistic effect between the CNFs and GNPs in addition to the formation of a well-connected percolating network. Such synergy in the hybrid composites is very beneficial for the design and development of future binder-free and lightweight electrodes to be used in flexible energy storage supercapacitors.

References

[1] Xiong, C., Li, B., Liu, H., Zhao, W., Duan, C., Wu, H. and Ni, Y., 2020. A smart porous wood-supported flower-like NiS/Ni conjunction with vitrimer co-effect as a multifunctional material with reshaping, shape-memory, and self-healing properties for applications in high-performance supercapacitors, catalysts, and sensors. *Journal of Materials Chemistry A*, *8*(21), pp.10898-10908.

[2] Bokhari, S.W., Siddique, A.H., Sherrell, P.C., Yue, X., Karumbaiah, K.M., Wei, S., Ellis, A.V. and Gao, W., 2020. Advances in graphene-based supercapacitor electrodes. *Energy Reports*, *6*, pp.2768-2784.

[3] Aval, L.F., Ghoranneviss, M. and Pour, G.B., 2018. High-performance supercapacitors based on the carbon nanotubes, graphene and graphite nanoparticles electrodes. *Heliyon*, *4*(11), p.e00862.

[4] Benoy, S.M., Pandey, M., Bhattacharjya, D. and Saikia, B.K., 2022. Recent trends in supercapacitor-battery hybrid energy storage devices based on carbon materials. Journal of Energy Storage, 52, p.104938.

[5] Ji, Y., Chen, F., Tan, S. and Ren, F., 2021. Hierarchical coral-like $MnCo_2O_{4.5}$@ Co–Ni LDH composites on Ni foam as promising electrodes for high-performance supercapacitor. Nanotechnology, 33(8), p.085402.

[6] Xu, B., Zheng, M., Tang, H., Chen, Z., Chi, Y., Wang, L., Zhang, L., Chen, Y. and Pang, H., 2019. Iron oxide-based nanomaterials for supercapacitors. Nanotechnology, 30(20), p.204002.

[7] Hussain, S., Amade, R., Boyd, A., Musheghyan-Avetisyan, A., Alshaikh, I., Martí-Gonzalez, J., Pascual, E., Meenan, B.J. and Bertran-Serra, E., 2021. Three-dimensional Si/vertically oriented graphene nanowalls composite for supercapacitor applications. *Ceramics International*, *47*(15), pp.21751-21758.

[8] Liu, H., Tao, Y., Sun, H., Wang, T.X., Peng, Z., Jin, J., Wang, Z., Peng, K., Wei, H., Li, Y.J. and Han, B.H., 2021. In-situ electrochemical polymerization of aniline on flexible conductive substrates for supercapacitors and non-enzymatic ascorbic acid sensors. Nanotechnology, 33(4), p.045405.

[9] Hussain, S., Kovacevic, E., Amade, R., Berndt, J., Pattyn, C., Dias, A., Boulmer-Leborgne, C., Ammar, M.R. and Bertran-Serra, E., 2018. Plasma synthesis of polyaniline enrobed carbon nanotubes for electrochemical applications. *Electrochimica Acta*, *268*, pp.218-225.

[10] Li, Z., Guo, D., Wang, D., Sun, M. and Sun, H., 2021. Exploration of Metal/Ti3C2 MXene-derived composites as anode for high-performance zinc-ion supercapacitor. Journal of Power Sources, 506, p.230197.

[11] Yu, L., Hu, L., Anasori, B., Liu, Y.T., Zhu, Q., Zhang, P., Gogotsi, Y. and Xu, B., 2018. MXene-bonded activated carbon as a flexible electrode for high-performance supercapacitors. *ACS Energy Letters*, *3*(7), pp.1597-1603.

[12] Cherusseri, J., Kumar, K.S., Choudhary, N., Nagaiah, N., Jung, Y., Roy, T. and Thomas, J., 2019. Novel mesoporous electrode materials for symmetric, asymmetric and hybrid supercapacitors. Nanotechnology, 30(20), p.202001.

[13] Patel, K.K., Singhal, T., Pandey, V., Sumangala, T.P. and Sreekanth, M.S., 2021. Evolution and recent developments of high performance electrode material for supercapacitors: a review. Journal of Energy Storage, 44, p.103366.

[14] Choi, J.H., Lee, C., Cho, S., Moon, G.D., Chang, H. and Jang, H.D., 2018. High capacitance and energy density supercapacitor based on biomass-derived activated carbons with reduced graphene oxide binder. Carbon, 132, pp.16-24.

[15] Xia, J., Chen, F., Li, J. and Tao, N., 2009. Measurement of the quantum capacitance of graphene. *Nature Nanotechnology*, *4*(8), pp.505-509.

[16] Cetinkaya, T. and Dryfe, R.A., 2018. Electrical double layer supercapacitors based on graphene nanoplatelets electrodes in organic and aqueous electrolytes: Effect of binders and scalable performance. *Journal of Power Sources*, *408*, pp.91-104.

[17] Cataldi, P., Athanassiou, A. and Bayer, I.S., 2018. Graphene nanoplatelets-based advanced materials and recent progress in sustainable applications. *Applied Sciences*, *8*(9), p.1438.

[18] Beidaghi, M., Wang, Z., Gu, L. and Wang, C., 2012. Electrostatic spray deposition of graphene nanoplatelets for high-power thin-film supercapacitor electrodes. *Journal of Solid State Electrochemistry*, *16*(10), pp.3341-3348.

[19] Singh, M.K., Suleman, M., Kumar, Y. and Hashmi, S.A., 2015. A novel configuration of electrical double layer capacitor with plastic crystal based gel polymer electrolyte and graphene nano-platelets as electrodes: a high rate performance. *Energy*, *80*, pp.465-473.

[20] Nath, N.C.D., Jeon, I.Y., Ju, M.J., Ansari, S.A., Baek, J.B. and Lee, J.J., 2019. Edge-carboxylated graphene nanoplatelets as efficient electrode materials for electrochemical supercapacitors. *Carbon*, *142*, pp.89-98.

[21] Al-Rubaye, S., Rajagopalan, R., Subramaniyam, C.M., Yu, Z., Dou, S.X. and Cheng, Z., 2016. Electrochemical performance enhancement in MnCo2O4 nanoflake/graphene nanoplatelets composite. *Journal of Power Sources*, *324*, pp.179-187.

[22] Bhattacharjya, D., Jeon, I.Y., Park, H.Y., Panja, T., Baek, J.B. and Yu, J.S., 2015. Graphene nanoplatelets with selectively functionalized edges as electrode material for electrochemical energy storage. *Langmuir*, *31*(20), pp.5676-5683.

[23] Ahmed, S., Rafat, M., Singh, M.K. and Hashmi, S.A., 2018. A free-standing, flexible PEDOT: PSS film and its nanocomposites with graphene nanoplatelets as electrodes for quasi-solid-state supercapacitors. Nanotechnology, 29(39), p.395401.

[24] Wang, K., Wang, Y., Wang, Y., Hosono, E. and Zhou, H., 2009. Mesoporous carbon nanofibers for supercapacitor application. The Journal of Physical Chemistry C, 113(3), pp.1093-1097.

[25] McDonough, J.R., Choi, J.W., Yang, Y., La Mantia, F., Zhang, Y. and Cui, Y., 2009. Carbon nanofiber supercapacitors with large areal capacitances. *Applied Physics Letters*, 95(24), p.243109.

[26] Kim, C. and Yang, K.S., 2003. Electrochemical properties of carbon nanofiber web as an electrode for supercapacitor prepared by electrospinning. *Applied physics letters*, 83(6), pp.1216-1218.

[27] Aydın, H., Kurtan, U., Demir, M. and Karakuş, S., 2022. Synthesis and Application of a Self-Standing Zirconia-Based Carbon Nanofiber in a Supercapacitor. Energy & Fuels, 36(4), pp.2212-2219.

[28] Jayawickramage, R.A.P., Balkus, K.J. and Ferraris, J.P., 2019. Binder free carbon nanofiber electrodes derived from polyacrylonitrile-lignin blends for high performance supercapacitors. Nanotechnology, 30(35), p.355402.

[29] Hérou, S., Bailey, J.J., Kok, M., Schlee, P., Jervis, R., Brett, D.J., Shearing, P.R., Ribadeneyra, M.C. and Titirici, M., 2021. High-Density Lignin-Derived Carbon Nanofiber Supercapacitors with Enhanced Volumetric Energy Density. Advanced Science, 8(17), p.2100016.

[30] Xu, B., Wang, H., Zhu, Q., Sun, N., Anasori, B., Hu, L., Wang, F., Guan, Y. and Gogotsi, Y., 2018. Reduced graphene oxide as a multi-functional conductive binder for supercapacitor electrodes. *Energy Storage Materials*, *12*, pp.128-136.

[31] Mohapatra, D., Badrayyana, S. and Parida, S., 2016. Designing binder-free, flexible electrodes for high-performance supercapacitors based on pristine carbon nano-onions and their composite with CuO nanoparticles. *RSC advances*, *6*(18), pp.14720-14729.

[32] Cheng, Q., Tang, J., Ma, J., Zhang, H., Shinya, N. and Qin, L.C., 2011. Graphene and carbon nanotube composite electrodes for supercapacitors with ultra-high energy density. Physical Chemistry Chemical Physics, 13(39), pp.17615-17624.

[33] Luo, J., Jang, H.D. and Huang, J., 2013. Effect of sheet morphology on the scalability of graphene-based ultracapacitors. ACS nano, 7(2), pp.1464-1471.

[34] Yasnur SK, Saha S, Ray A, Das M, Mukherjee A, and Das S., 2021. Effect of electrolyte concentration on electrochemical performance of bush like α-Fe_2O_3 nanostructures. *ChemistrySelect*, 6, 9823– 9832.

[35] Daraghmeh, A., Hussain, S., Haq, A.U., Saadeddin, I., Servera, L. and Ruiz, J.M., 2020. Carbon nanocomposite electrodes for electrical double layer capacitor. *Journal of Energy Storage*, *32*, p.101798.

[36] Daraghmeh, A., Hussain, S., Servera, L., Xuriguera, E., Cornet, A. and Cirera, A., 2017. Impact of binder concentration and pressure on performance of symmetric CNFs based supercapacitors. *Electrochimica Acta*, *245*, pp.531-538.

[37] Daraghmeh, A., Hussain, S., Saadeddin, I., Servera, L., Xuriguera, E., Cornet, A. and Cirera, A., 2017. A study of carbon nanofibers and active carbon as symmetric supercapacitor in aqueous electrolyte: a comparative study. Nanoscale research letters, 12(1), pp.1-10.

[38] Afzal, U., Aslam, M., Afzal, F., Maryam, K., Ahmad, N., Zafar, Q. and Farooq, Z., 2022. Fabrication of a graphene-based sensor to detect the humidity and the temperature of a metal body with imprecise data analysis. RSC advances, 12(33), pp.21297-21308.

[39] Ghouri, Z.K., Barakat, N.A., Alam, A.M., Park, M., Han, T.H. and Kim, H.Y., 2015. Facile synthesis of Fe/CeO2-doped CNFs and their capacitance behavior. International Journal of Electrochemical Science, 10(3), pp.2064-2071.

[40] Susantyoko, R.A., Parveen, F., Mustafa, I. and Almheiri, S., 2019. MWCNT/activated-carbon freestanding sheets: a different approach to fabricate flexible electrodes for supercapacitors. *Ionics*, *25*(1), pp.265-273.

[41] Murugan, M., Dineshkumar, G., Kumar, K.C., Tewari, C., Ganesan, M., Sahoo, N.G. and Sivanantham, M., 2023. Development of Mesoporous Carbon Composites with Waste Plastics Derived Graphene and MnO2 for Supercapacitor Applications. Journal of The Electrochemical Society, 170(4), p.040518.

[42] Fikry, M., Abbas, M., Sayed, A., Nouh, A., Ibrahim, A. and Mansour, A.S., 2022. Using a novel graphene/carbon nanotubes composite for enhancement of the supercapacitor electrode capacitance. Journal of Materials Science: Materials in Electronics, 33(7), pp.3914-3924.

[43] Ab Rahim, A.H., Ramli, N., Nordin, A.N. and Abd Wahab, M.F., 2021. Supercapacitor performance with activated carbon and graphene nanoplatelets composite electrodes, and insights from the equivalent circuit model. Carbon Trends, 5, p.100101.

[44] Yu, S., Li, Y. and Pan, N., 2014. KOH activated carbon/graphene nanosheets composites as high performance electrode materials in supercapacitors. RSC Advances, 4(90), pp.48758-48764.

[45] Cheng, F., Yang, X., Dai, S., Song, D., Zhang, S. and Lu, W., 2020. Interweaving activated carbon with multi-dimensional carbon nanomaterials for high-performance supercapacitors. Journal of The Electrochemical Society, 167(4), p.040507.

[46] Rapisarda, M., Damasco, A., Abbate, G. and Meo, M., 2020. Carbon black and reduced graphene oxide nanocomposite for binder-free supercapacitors with reduced graphene oxide paper as the current collector. ACS omega, 5(50), pp.32426-32435.

[47] Pappu, S., Nanaji, K., Mandati, S., Rao, T.N., Martha, S.K. and Bulusu, S.V., 2020. Cost-Effective Synthesis of Electrodeposited $NiCo_2O_4$ Nanosheets with Induced Oxygen Vacancies: A Highly Efficient Electrode Material for Hybrid Supercapacitors. Batteries & Supercaps, 3(11), pp.1209-1219.

[48] Bhattacharya, G., Fishlock, S.J., Pritam, A., Sinha Roy, S. and McLaughlin, J.A., 2020. Recycled red mud–decorated porous 3D graphene for high-energy flexible micro-supercapacitor. Advanced Sustainable Systems, 4(4), p.1900133.

[49] Bhattacharya, G., Fishlock, S.J., Roy, J.S., Pritam, A., Banerjee, D., Deshmukh, S., Ghosh, S., McLaughlin, J.A. and Roy, S.S., 2019. Effective utilization of waste red mud for high performance supercapacitor electrodes. Global Challenges, 3(2), p.1800066.

[50] Dong, L., Xu, C., Yang, Q., Fang, J., Li, Y. and Kang, F., 2015. High-performance compressible supercapacitors based on functionally synergic multiscale carbon composite textiles. Journal of Materials Chemistry A, 3(8), pp.4729-4737.

[51] Stoller, M.D. and Ruoff, R.S., 2010. Best practice methods for determining an electrode material's performance for ultracapacitors. *Energy & Environmental Science*, 3(9), pp.1294-1301.

[52] Gong, Y., Li, D., Fu, Q. and Pan, C., 2015. Influence of graphene microstructures on electrochemical performance for supercapacitors. *Progress in Natural Science: Materials International*, *25*(5), pp.379-385.

[53] Bhattacharya, G., Mathur, A., Pal, S., McLaughlin, J. and Roy, S.S., 2016. Equivalent circuit models and analysis of electrochemical impedance spectra of caffeine solutions and beverages. Int J Electrochem Sci, 11, pp.6370-86.

[54] Schütter, C., Ramirez-Castro, C., Oljaca, M., Passerini, S., Winter, M. and Balducci, A., 2014. Activated carbon, carbon blacks and graphene based nanoplatelets as active materials for electrochemical double layer capacitors: a comparative study. *Journal of the Electrochemical Society*, *162*(1), p.A44.

[55] Prawoto, Y., Djuansjah, J.R.P. and Shaffiar, N.B., 2012. Re-visiting the 'rule of mixture' used in materials with multiple constituting phases: A technical note on morphological considerations in austenite case study. Computational materials science, 65, pp.528-535.

[56] Szeluga, U., Kumanek, B. and Trzebicka, B., 2015. Synergy in hybrid polymer/nanocarbon composites. A review. Composites Part A: Applied Science and Manufacturing, 73, pp.204-231.

[57] Higgins, T.M., McAteer, D., Coelho, J.C.M., Sanchez, B.M., Gholamvand, Z., Moriarty, G., McEvoy, N., Berner, N.C., Duesberg, G.S., Nicolosi, V. and Coleman, J.N., 2014. Effect of percolation on the capacitance of supercapacitor electrodes prepared from composites of manganese dioxide nanoplatelets and carbon nanotubes. ACS nano, 8(9), pp.9567-9579.

[58] Stauffer, D. and Aharony, A., 2018. Introduction to percolation theory. Taylor & Francis.

[59] Wu, N.L. and Wang, S.Y., 2002. Conductivity percolation in carbon–carbon supercapacitor electrodes. Journal of power sources, 110(1), pp.233-236.

[60] Marsden, A.J., Papageorgiou, D.G., Valles, C., Liscio, A., Palermo, V., Bissett, M.A., Young, R.J. and Kinloch, I.A., 2018. Electrical percolation in graphene–polymer composites. 2D Materials, 5(3), p.032003.

[61] Zhao, Y., Hao, M., Wang, Y., Sha Y., Su L. Effect of electrolyte concentration on the capacitive properties of NiO electrode for supercapacitors. J Solid State Electrochem 20, 81–85 (2016).

[62] Krishnan, P. and Biju, V., 2021. Effect of electrolyte concentration on the electrochemical performance of RGO–KOH supercapacitor. Bulletin of Materials Science, 44, pp.1-11.